Ultra-Wideband Nonstationary Channel Modeling for UAV-to-Ground Communications

Boyu Hua[1], Liwei Han[1], Qiuming Zhu[1], Cheng-Xiang Wang[1], Kai Mao[1], Junwei Bao[1], Hengtai Chang[1], and Zhenzhou Tang[1]

[1]Affiliation not available

December 09, 2024

Ultra-Wideband Nonstationary Channel Modeling for UAV-to-Ground Communications

Boyu Hua, *Member, IEEE*, Liwei Han, Qiuming Zhu, *Senior Member, IEEE,* Cheng-Xiang Wang, *Fellow, IEEE,*
Kai Mao, Junwei Bao, Hengtai Chang, *Member, IEEE*, Zhenzhou Tang, *Member, IEEE*

***Abstract*—Unmanned aerial vehicle (UAV)-to-ground (U2G) channel models play a decisive role in the design, optimization, and evaluation of communication systems between UAV and ground terminal. This paper proposes a three-dimensional (3D) model for U2G communication channels, enhanced with ultra-wideband (UWB) features and frequency non-stationarity. This model integrates large-scale and small-scale fading components, introducing bandwidth-dependent path numbers and the UAV posture matrix for realistic scenario representation. It encompasses specific UWB U2G channel phenomena such as the channel hardening, UAV 3D movements, and posture variation effect. The channel parameters, including spatial large-scale parameters (LSPs), bandwidth-correlated path numbers, delay-posture-correlated path power, and frequency-correlated path phase, are generated to capture channel non-stationary characteristics across time and frequency domains. Employing ray-tracing (RT) for the path number and optimization methods for the path delay, the proposed model ensures reliable parameter evolution. The proposed model is assessed through key statistical properties, including space-time-frequency correlation functions, power delay profile, root-mean-square delay spread, Doppler power spectrum density, and the energy variance. It is demonstrated that both posture and bandwidth variations have crucial effects on channel characteristics. The validity and practicability of this research is demonstrated by comparing the simulated outcomes with the measurement data.**

***Index Terms*—UAV, Channel model, UWB, Non-stationary, Posture variation.**

I. INTRODUCTION

A. Motivations

THE increasing deployment of unmanned aerial vehicles (UAVs) across diverse sectors, including photography, traffic surveillance, telecommunication, and logistics, underscores their growing significance. UAVs, as versatile aerial platforms, boast numerous advantages such as cost-efficiency, ease of operation, and exceptional adaptability to varied environments, making them as an optimal solution for air-to-ground (A2G) wireless communication. Unlike conventional ground-based communication networks, UAV-enabled communication systems emerge as a compelling alternative for facilitating emergency search and rescue missions. The inherent elevated positioning of UAVs enhances the likelihood of establishing direct line-of-sight (LoS) connections, thereby ensuring more stable and reliable communication links for UAV-to-ground (U2G) communications. Concurrently, ultrawide bandwidth (UWB) technology marks a significant evolution in wireless communication, distinguished by its adoption of a broad frequency spectrum [1], [2]. The IEEE 802.15.4z standard delineates an ultra-wide bandwidth, encompassing nearly 5 GHz [3], which not only supports high data transfer rates but also provides enhanced spatial resolution, making UWB exceptionally suitable for U2G communication scenarios [4], [5].

The efficacy of communication systems is intimately tied to channel stability, highlighting the necessity of robust channels for the uninterrupted flow of information. In the realm of UAV-assisted communication systems, the development of accurate and realistic channel models is imperative for effective system analysis and design. Unique to UWB UAV communication are its distinct attributes, such as a broad frequency spectrum, varying flight altitudes, advanced maneuverability, three-dimensional (3D) orientations, and the posture variation [6]–[8]. Despite these advancements, research on the specific characteristics of UAV channels within UWB contexts remains markedly scant, presenting an urgent requirement for further exploration and discovery.

B. Related Works

Channel modeling approaches for the U2G communication scenarios are broadly classified into statistical, geometrical, and machine learning (ML)-based frameworks [9], [10]. Statistical modeling constructs channel representations by relying on key empirical parameters, often derived from extensive measurements or sophisticated ray-tracing (RT) simulations [11]. However, these models face challenges in capturing space-time continuity comprehensively, making them more suitable for segmented analysis or link-level studies [12]. To address the shortcomings of purely statistical approaches, geometry-based stochastic models (GBSMs) incorporate geometric principles

---

This work was supported by the National Key R&D Program of China (2022YFB2903600), the National Natural Science Foundation of China (62271250 and 61960206006), the Key Technologies R&D Program of Jiangsu (Prospective and Key Technologies for Industry) (BE2022067, BE2022067-3 and BE2022067-1), the Natural Science Foundation of Jiangsu Province (BK20211182). (*Corresponding author: Q. Zhu, C.-X. Wang*)

Boyu Hua, Liwei Han, Qiuming Zhu, Kai Mao are with the College of Electronic and Information Engineering, Nanjing University of Aeronautics and Astronautics, Nanjing 211106, China (e-mail: byhua@nuaa.edu.cn, zhuqiuming@nuaa.edu.cn).

Cheng-Xiang Wang is with the National Mobile Communications Research Laboratory, Southeast University, Nanjing 210096, China, and also with the Pervasive Communication Research Center, Purple Mountain Laboratories, Nanjing 211111, China (e-mail: chxwang@seu.edu.cn).

Junwei Bao is with the Department of Physics, Nanjing University of Aeronautics and Astronautics, Nanjing, 210016, China.

Hengtai Chang is with the School of Information Science and Engineering, Shandong University, Qingdao 266237, China. (e-mail: changht@sdu.edu.cn).

Zhenzhou Tang is with the National Key Laboratory of Microwave Photonics, Nanjing University of Aeronautics and Astronautics, Nanjing, 210016, China (e-mail: tangzhzh@nuaa.edu.cn).

to accurately determine scatterer configurations and locations, enhancing the spatial and temporal resolution. GBSMs employ regular or irregular geometrical shapes to represent diverse scattering environments [13]–[15]. For example, the authors in [16] utilized a prolate spheroidal coordinate system for non-stationary mobile-to-mobile channels, providing the joint delay-Doppler probability density function. Additionally, the authors in [17] introduced a GBSM tailored for uncorrelated scattering Rayleigh fading channels, which adeptly captured the temporal evolution of signal and analyzed quasi-stationary intervals. ML-based channel models leverage the correlations between different channel parameters to facilitate comprehensive multidimensional analysis [18], [19]. These approaches utilize both supervised and unsupervised learning algorithms to predict channel parameters and classify scenarios, with their performance critically dependent on the quality and extent of the training datasets [20], [21]. The future of channel modeling lies in the integration of these diverse methodologies, combining the strengths of various modeling approaches to develop more robust and versatile channel models.

In contrast to conventional communication terminals, UAVs possess distinctive characteristics such as arbitrary motion and postures, which add complexity to the wireless channel. For instance, the authors in [22] examined the effects of UAV height and trajectories on the channel non-stationarity. The authors in [23] investigated 3D trajectories and introduced a beam channel model. A GBSM was proposed in [24] and [25] to evaluate the impact of UAV rotation, highlighting its influence on statistical properties and non-stationarity. The effects of airframe shadowing, caused by the UAV's structure and posture, can be addressed in [26]. However, these analyses are limited to single-angle posture changes. Furthermore, the authors in [27]–[29] presented stochastic models exploring specific posture variations and their impact on temporal channel correlation, though they focused on wobbling effects rather than arbitrary 3D postures. A hybrid channel model for U2G communications was introduced in [30], incorporating arbitrary trajectory and 3D posture variation fading. Despite these contributions, the effects of 3D posture on the power and phase of multi-input-multi-output (MIMO) channels remain unexplored.

Numerous investigations have been undertaken to assess the impact of UWB characteristics on channel behavior and to formulate corresponding models. The work in [31] focused on A2G UWB channel analysis, modeling the received power and path losses. The authors in [32] explored the large- and small-scale attributes of UWB A2G channels via empirical measurements. The studies in [33], [34] executed UWB measurements and modeling, with an emphasis on multipath analysis. Further, [35] extended UWB channel modeling to span 3-18 GHz, addressing both LoS and multipath components. The research conducted in [36] explored UWB channel sound measurements and modeling within mmWave and sub-mmWave bands, specifically for wagon channel characterization. However, these UWB studies were mainly based on the assumption of wide-sense stationarity. The authors in [30] provided measured stationary interval results under different roll angles, which could validate the non-stationary characteristics of UAV channel. In [37], the authors conducted measurements of UAV-to-ground channels, and analyzed the coherence bandwidth, demonstrating the non-stationary characteristics. Specifically, the authors in [38] identified the presence of frequency domain non-stationarity and channel hardening phenomena in wireless channels. For various bandwidths, the authors in [39] developed a space-time-frequency channel model based on empirical data. Moreover, the authors in [40] introduced a pervasive channel model to address non-stationarity, yet did not define bandwidth-dependent parameters. While these studies have established significant groundwork, a comprehensive modeling approach that fully incorporates UWB characteristics and frequency domain non-stationarity is still lacking.

These identified gaps underscore the necessity of developing a UWB non-stationary U2G channel model that captures the unique characteristics of UAVs and the UWB communication systems, incorporating a more authentic channel parameter generation and time-frequency evolution approach. This paper aims to bridge these research gaps.

C. Contributions

Motivated by the existing research landscape and identified gaps, this paper proposes a comprehensive channel model that integrates the geometrical details, the RT approach, and the optimization method to accurately represent the UWB and distinct aspects of the U2G communication scenario. The primary contributions and innovations of this work are delineated as follows.

1) We propose a non-stationary U2G multi-input-multi-output channel model supporting UWB and UAV-specific features. This model addresses both large-scale and small-scale fading effects, and provides bandwidth-dependent path and sub-path numbers to reflect channel hardening phenomena in UWB scenarios. A modified expression for motion-induced equivalent Doppler phase is introduced to address the frequency-variant effect across ultrawide bandwidth. Additionally, the model accounts for variations in UAV posture through path power modification, ensuring the structural characteristics of UAV are integrated into the analysis. These enhancements collectively yield a more precise depiction of the communication channel.

2) Generation and time-frequency-evolution procedure of channel parameters are given. Built on spatial correlation, the model integrates frequency-dependent and bandwidth-dependent factors to align large-scale-parameters (LSPs) with UWB attributes. The RT method provides abundant data for investigating the impact of bandwidth on the path and sub-path numbers. Subsequently, an optimization technique is utilized to calculate and evolve path power, considering the path delay and UAV posture. Furthermore, methodologies for calculating and updating frequency-variant equivalent Doppler phases are presented. These calculation procedures facilitate the spatial-temporal-frequency stable evolution of channel parameters.

3) Statistical properties of the proposed UWB U2G channel model are given and analyzed, including spatial-temporal-frequency correlation functions (CFs), power delay profile

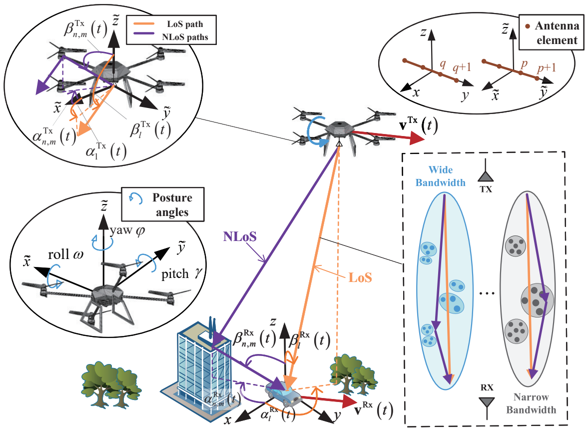

Fig. 1. Illustration of the UWB channel model for U2G communication.

(PDP), root mean square delay spread (RMS-DS), and Doppler power spectral density (DPSD). Through comprehensive simulations, the statistical characteristics of UWB U2G channels are analyzed, examining the impact of bandwidth on temporal correlation function (TCF), frequency correlation function (FCF), PDP, and DPSD. The concept of energy variance (EV) is defined to quantify channel hardening effects, with a detailed discussion on the impact of varying K-factors on EV. Additionally, the validity and accuracy of the proposed model are further affirmed through the measurement verification of the RMS-DS, K-factor, and received power across different flight height and bandwidths.

The remainder of this paper is organized as follows. Section II describes a UWB non-stationary U2G channel model incorporating 3D motion and posture variation. Section III studies the generation and time-frequency-evolution of the model parameters. Statistical properties of proposed model are presented and analyzed in Section IV. Section V discusses and compares the simulated and measured results. Conclusions are finally drawn in Section VI.

II. ULTRA-WIDEBAND U2G CHANNEL MODEL

The illustration of the proposed channel model is shown in Fig. 1, where only the LoS path and the m^{th} sub-path in the n^{th} scattering path between the p^{th} transmitter (Tx) and q^{th} receiver (Rx) are shown for clarity. The model accommodates UWB characteristics, resulting in variable scattering cluster properties across bandwidths. Specifically, as depicted, wider bandwidth channels exhibit an increased number of scattering clusters but a reduced number of rays within each cluster compared to narrower bandwidths. This phenomenon is attributed to the wider bandwidth enhanced delay resolution, which distinguishes previously indiscernible multipath components. Moreover, the signal propagation paths associated with scattering clusters are termed paths, and the internal rays are referred to as sub-paths.

The UWB MIMO fading channel between UAV and the ground terminal is affected by both large-scale fading and small-scale fading, thus a channel matrix with P transmitting antenna elements and Q receiving antenna elements can be expressed as

$$[H]_{P\times Q}=\sqrt{L_{f_c}^{\mathrm{PL}}(d,B)\,L_{f_c}^{\mathrm{SF}}(B)}\cdot\left[h_{pq,f_c}(t,\tau,B)\right]_{P\times Q} \tag{1}$$

where B is the practical signal bandwidth, f_c and f'_c denotes the carrier wave frequency and the center frequency of the signal, L_{PL} represents the path loss (PL), and L_{SF} denotes the shadowing fading (SF). The variables related to bandwidth, including L_{PL}, L_{SF}, and $h_{pq,f_c}(t,\tau,B)$, are obtained by integrating frequency-related component over f. Taking PL as an example, our proposed method can be expressed as

$$L_{f_c}^{\mathrm{PL}}(d,B)=\frac{\int_{f_c-\frac{B}{2}}^{f_c+\frac{B}{2}}L_f^{\mathrm{PL}}(d)\,df}{B} \tag{2}$$

where $L_f^{\mathrm{PL}}(d)$ is the path loss with the respect of f and d. This approach captures the precise channel characteristics across the bandwidth, addressing the limitations of traditional narrowband models. Note that if the channel parameter remains uniform across the bandwidth, the proposed model reduced to the traditional one.

To accurately capture the time-frequency variant small-scale fading, the channel impulse response (CIR) between the p^{th} transmitting antenna element and the q^{th} receiving antenna element is modeled as

$$\begin{aligned}h_{pq,f_c}(t,\tau,B)=&\sqrt{\frac{K_{f_c}(t,B)}{K_{f_c}(t,B)+1}}\int_{f_c-\frac{B}{2}}^{f_c+\frac{B}{2}}\frac{h_{pq,f}^{\mathrm{L}}(t)}{B}df\,\delta(\tau-\tau_{pq}^{\mathrm{L}}(t))\\&+\sqrt{\frac{1}{K_{f_c}(t,B)+1}}\sum_{n=1}^{N(t,B)}\sum_{m=1}^{M_n}\int_{f_c-\frac{B}{2}}^{f_c+\frac{B}{2}}\frac{h_{pq,f,n_m}^{\mathrm{NL}}(t)}{B}df\,\delta(\tau-\tau_{pq,n_m}^{\mathrm{NL}}(t))\end{aligned} \tag{3}$$

where $K_{f_c}(t,B)$ denotes the Rician factor, $\tau_{pq}^{\mathrm{L}}(t)$and $\tau_{pq,n_m}^{\mathrm{NL}}(t)$ denote the delays of the LoS and the non-line-of-sight (NLoS) paths, respectively. $N(t,B)$ is the total number of paths after clustering, and M_n is the number of sub-paths within the n^{th} path. Generally, higher bandwidth leads to a larger $N(t,B)$. The coefficients $h_{pq,f}^{\mathrm{L}}(t)$ and $h_{pq,f,n_m}^{\mathrm{NL}}(t)$ can be further modeled as

$$h_{pq,f}^{\mathrm{L}}(t)=F_{pq}^{\mathrm{L}}(t)\,C_{pq}^{\mathrm{L}}(t)\,e^{\mathrm{j}\Phi_{pq,f}^{\mathrm{L}}(t)} \tag{4}$$

$$h_{pq,f,n_m}^{\mathrm{NL}}(t)=F_{pq}^{\mathrm{NL}}(t)\,C_{pq,n_m}^{\mathrm{NL}}(t)\,e^{\mathrm{j}\Phi_{pq,f,n_m}^{\mathrm{NL}}(t)} \tag{5}$$

where $C_{pq}^{\mathrm{L}}(t)$ denotes the power modification factor due to the obstruction by airframe structure, C_{pq,n_m}^{NL} is the power modification factor related to path delays, $e^{\mathrm{j}\Phi_{pq,f}^{\mathrm{L}}(t)}$ and $e^{\mathrm{j}\Phi_{pq,f,n_m}^{\mathrm{NL}}(t)}$ denote the motion-induced equivalent Doppler phase of LoS and NloS paths, respectively. $F_{pq}^{\mathrm{L}}(t)$ and $F_{pq}^{\mathrm{NL}}(t)$ denote the antenna pattern function that take into account the posture variation, which can be further defined as

$$F_{pq}^{\mathrm{L}}(t)=\begin{bmatrix}F_{p,\mathrm{V}}^{\mathrm{T}}(\mathbf{s}_l^{\mathrm{T}}(t),\mathbf{R}^{\mathrm{P}}(t))\\F_{p,\mathrm{H}}^{\mathrm{T}}(\mathbf{s}_l^{\mathrm{T}}(t),\mathbf{R}^{\mathrm{P}}(t))\end{bmatrix}^{\mathrm{T}}\begin{bmatrix}e^{\mathrm{j}\Phi_l^{\mathrm{VV}}}&0\\0&e^{\mathrm{j}\Phi_l^{\mathrm{HH}}}\end{bmatrix}\begin{bmatrix}F_{q,\mathrm{V}}^{\mathrm{R}}(\mathbf{s}_l^{\mathrm{R}}(t),\mathbf{R}^{\mathrm{P}}(t))\\F_{q,\mathrm{H}}^{\mathrm{R}}(\mathbf{s}_l^{\mathrm{R}}(t),\mathbf{R}^{\mathrm{P}}(t))\end{bmatrix} \tag{6}$$

$$\begin{aligned}F_{pq}^{\mathrm{NL}}(t)=&\begin{bmatrix}F_{p,\mathrm{V}}^{\mathrm{T}}(\mathbf{s}_{n_m}^{\mathrm{T}}(t),\mathbf{R}^{\mathrm{P}}(t))\\F_{p,\mathrm{H}}^{\mathrm{T}}(\mathbf{s}_{n_m}^{\mathrm{T}}(t),\mathbf{R}^{\mathrm{P}}(t))\end{bmatrix}^{\mathrm{T}}\begin{bmatrix}e^{\mathrm{j}\Phi_{n_m}^{\mathrm{VV}}}&\sqrt{\kappa_{n_m}^{-1}}e^{\mathrm{j}\Phi_{n_m}^{\mathrm{VH}}}\\\sqrt{\kappa_{n_m}^{-1}}e^{\mathrm{j}\Phi_{n_m}^{\mathrm{HV}}}&e^{\mathrm{j}\Phi_{n_m}^{\mathrm{HH}}}\end{bmatrix}\\&\begin{bmatrix}F_{q,\mathrm{V}}^{\mathrm{R}}(\mathbf{s}_{n_m}^{\mathrm{R}}(t),\mathbf{R}^{\mathrm{P}}(t))\\F_{q,\mathrm{H}}^{\mathrm{R}}(\mathbf{s}_{n_m}^{\mathrm{R}}(t),\mathbf{R}^{\mathrm{P}}(t))\end{bmatrix}\end{aligned} \tag{7}$$

where $F_{p/q,\mathrm{V}}^{\mathrm{T/R}}(\cdot)$ and $F_{p/q,\mathrm{H}}^{\mathrm{T/R}}(\cdot)$ denote the antenna pattern components of Tx or Rx in vertical and horizontal planes,

TABLE I: Definitions of Key Channel Parameters

Parameters	Definitions	Parameters	Definitions
B	Practical signal bandwidth	$F_{pq}^{\mathrm{L}}(t)$, $F_{pq}^{\mathrm{NL}}(t)$	Antenna pattern functions
f,f_c	Different frequency within the bandwidth and center frequency of the signal	$F_{p/q,\mathrm{V}}^{\mathrm{T/R}}(\cdot)$, $F_{p/q,\mathrm{H}}^{\mathrm{T/R}}(\cdot)$	Antenna pattern components of Tx or Rx in vertical and horizontal planes
$L_{f_c}^{\mathrm{PL}}(d,B)$, $L_{f_c}^{\mathrm{SF}}(B)$	Path loss and shadow fading	$\mathbf{s}_l^{T/R}(t)$, $\mathbf{s}_{n,m}^{T/R}(t)$	Angle unit vectors of LoS and NLoS paths at the Tx and Rx
$K_{f_c}(t,B)$	Time-frequency-variant Rician K-factor	$\Phi_{\mathrm{T/R}}^{\mathrm{VV/HH}}$, $\Phi_{\mathrm{T/R}}^{\mathrm{VH/HV}}$	Initial phases for different polarizations
$\tau_{pq}^{\mathrm{L}}(t)$, $\tau_{pq,n_m}^{\mathrm{NL}}(t)$	Delays of the LoS and NLoS path	B_s, f_s	Bandwidth and central frequency of the channel sub-interval
$N(t,B)$, M_n	Number of paths and sub-paths	$C_{pq}^{\mathrm{L}}(t)$, $C_{pq,n_m}^{\mathrm{NL}}(t)$	Power modification factor
$\Phi_{\mathrm{D},pq,f/\mathrm{D},pq,f,n_m}^{\mathrm{L/NL}}(t)$, $\Phi_{\mathrm{A},pq,f/\mathrm{A},pq,f,n_m}^{\mathrm{L/NL}}(t)$	Traditional Doppler effect component and the posture variation component	$\mathbf{s}_l^{\mathrm{T}}(t)$, $\mathbf{s}_l^{\mathrm{R}}(t)$, $\mathbf{s}_{n_m}^{\mathrm{T}}(t)$, $\mathbf{s}_{n_m}^{\mathrm{R}}(t)$	Angle unit vectors for the LoS and NLoS paths at Tx and Rx
$\phi_{x/y}^{\mathrm{T}}$, $\phi_{x/y}^{\mathrm{R}}$	Azimuth angle of departure and arrival	f_d^{L}, f_d^{NL}	Equivalent Doppler frequency of the LoS and NLoS
$\mathbf{e}_p(t)$, $\mathbf{e}_q(t)$	Vector pointing to the antenna element from Tx and Rx	$\mathbf{L}^{T/R}(t_0)$	Initial location of Tx and Rx
$\mathbf{R}^{\mathrm{R}}(t)$, $\mathbf{R}^{\mathrm{P}}(t)$	Velocity rotation matrix and posture matrix	$\alpha_l^{\mathrm{T/R}}(t)$, $\beta_l^{\mathrm{T/R}}(t)$	AAoD or AAOA and EAoA or EAOA of LoS
$\alpha_{n_m}^{\mathrm{T//R}}(t)$, $\beta_{n_m}^{\mathrm{T/R}}(t)$	AAoD or AAOA and EAoD or EAOA of NLoS	ω, φ, γ	Roll, yaw, and pitch angles

respectively, $\mathbf{s}_l^{\mathrm{T/R}}(t)$ and $\mathbf{s}_{n,m}^{\mathrm{T/R}}(t)$ are the unit vectors of LoS and NLoS paths at the Tx or Rx, and determined by the angles of departure and arrival. $\mathbf{R}^{\mathrm{P}}(t)$ is the posture matrix which will be discussed in next chapter, $\Phi_{l/n_m}^{\mathrm{VV}}$, $\Phi_{l/n_m}^{\mathrm{HH}}$, $\Phi_{l/n_m}^{\mathrm{VH}}$ and $\Phi_{l/n_m}^{\mathrm{HV}}$ are initial phases for different polarization combinations, which describe the polarization phase variation for LoS and NLoS paths, and $\kappa_{n,m}$ is the cross-polarization power ratio.

To simulate the proposed UWB models and facilitate the computation of the integral calculation, a method to transform the integral into a summation of intervals are employed. The channel transfer function (CTF) can be obtained by performing the Fourier transform of CIR over the whole bandwidth as

$$
\begin{aligned}
&H_{pq,f_c}(t,f,B) = \int_0^{+\infty} h_{pq,f_c}(t,\tau,B)e^{-j2\pi f\tau}d\tau \\
=&\frac{F_{pq}^{\mathrm{L}}(t)C_{pq}^{\mathrm{L}}(t)}{B}\sqrt{\frac{K_{f_c}(t,B)}{K_{f_c}(t,B)+1}}\int_{f_c-\frac{B}{2}}^{f_c+\frac{B}{2}} e^{j\Phi_{pq,f'}^{\mathrm{L}}(t)-j2\pi f\tau_{pq}^{\mathrm{L}}(t)}df' \\
&+\frac{F_{pq}^{\mathrm{NL}}(t)}{B}\sqrt{\frac{1}{K_{f_c}(t,B)+1}}\int_{f_c-\frac{B}{2}}^{f_c+\frac{B}{2}}\sum_{n=1}^{N(t,B)}\sum_{m=1}^{M_n}C_{pq,n_m}^{\mathrm{NL}}(t) \\
&\cdot e^{j\Phi_{pq,f',n_m}^{\mathrm{NL}}(t)-j2\pi f\tau_{pq,n_m}^{\mathrm{NL}}}df'
\end{aligned}
\tag{8}
$$

Note that f is the frequency variable for Fourier transform in (8), and $f^{'}$ is used for integration to derive the channel characteristics in the frequency domain. This formulation captures the key contributions to the UWB channel properties, including the Rician factor, the phase of LoS path, and the phases of NLoS sub-paths. Moreover, these factors play a critical role in the unique channel characteristics over the ultra-wide frequency range.

When the bandwidth narrows, channel parameters within this bandwidth remain relatively stable across different frequencies, suggesting that modeling the channel at its central frequency is sufficient for narrowband characterization. This observation implies a simplification of the UWB model to a conventional narrowband model under certain conditions.

In the proposed model, all frequency-variant parameters contribute to frequency non-stationarity. Furthermore, the parameter calculation approach within a given bandwidth ensures that this non-stationarity is accurately captured. Consequently, the model effectively accounts for the comprehensive non-stationarity arising from the time-varying characteristics of UAVs and the pronounced frequency dependence inherent in UWB communication.

III. CHANNEL PARAMETERS GENERATION AND EVOLUTION

A. *Spatial-frequency-bandwidth-correlated LSPs*

The generation and temporal evolution of channel parameters are crucial for constructing an accurate channel model. By thoroughly considering variables such as velocity, signal bandwidth, and UAV posture angle, we generate realistic parameters including path angles, phases, delays, and powers. Fig. 2 presents the detailed flowchart of the proposed channel generation process.

LSPs play a pivotal role in characterizing large-scale channel fading, which is generally stable over several meters of movement. For instance, SF results from obstructions like buildings or trees that block a substantial portion of the signal.

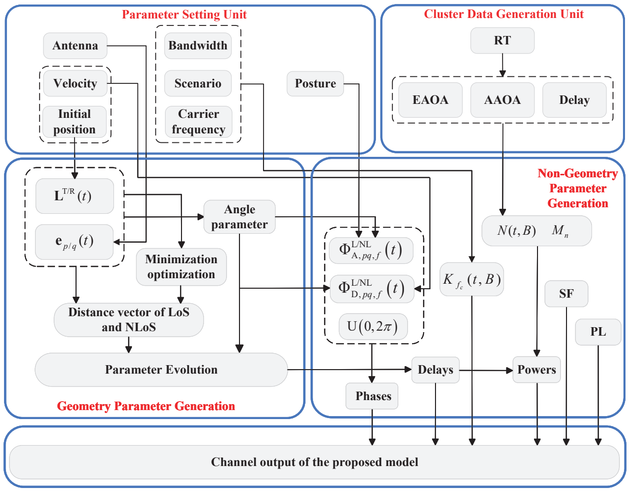

Fig. 2. Flowchart of the proposed channel generation process.

The decorrelation distance for SF, i.e., the minimum distance a mobile terminal must move to encounter a noticeable change in SF, is approximately equal to the dimensions of the obstructing objects. Consequently, when a mobile terminal follows a specific path or when multiple terminals are positioned in close proximity, their LSPs exhibit correlation with respect to locations of Tx and Rx.

Moreover, the positioning and reflective attributes of scattering clusters depend on several LSPs, including SF, Rician factor, path delay spread, azimuth or elevation spread of departure, azimuth or elevation spread of arrival, and cross-polarization ratio. Typically, these LSPs follow specific distributions, derived directly from empirical measurement data. For example, the Rician factor $K_{f_c}(t,B)$ is modeled as a Lognormal process within a given bandwidth B (GHz). Given the positions of Tx and Rx as $\mathbf{p} = \left(x^{\mathrm{T}}(t), y^{\mathrm{T}}(t), z^{\mathrm{T}}(t), x^{\mathrm{R}}(t), y^{\mathrm{R}}(t), z^{\mathrm{R}}(t)\right)$, the Rician factor can be generated by

$$\begin{aligned} K_{f_c}(t,B) = {} & K_{\mu} + \int_{f_\mathrm{c}-\frac{B}{2}}^{f_\mathrm{c}+\frac{B}{2}} K_{\gamma} \log_{10}(\omega_{\mathrm{ref}} + f) df + K_{\varepsilon} \log_{10} B \\ & + X^{K}(\mathbf{p}) \left[K_{\sigma} + \int_{f_\mathrm{c}-\frac{B}{2}}^{f_\mathrm{c}+\frac{B}{2}} K_{\delta} \log_{10}(\omega_{\mathrm{ref}} + f_c) df + K_{\kappa} \log_{10} B \right] \end{aligned} \tag{9}$$

where K_{μ} and K_{σ} are the reference mean value and the reference standard deviation at a carrier frequency of 1 GHz, respectively, ω_{ref} is the reference frequency offset in GHz, K_{γ} and K_{ϵ} are frequency-dependence and bandwidth-dependence constant, respectively, K_{δ} and K_{κ} are the frequency-dependence and bandwidth-dependence of the reference standard deviation, respectively. Additionally, $X^{K} \sim \mathcal{N}(0,1)$ is a spatially correlated Gaussian random variable with a zero mean and unit variance, which is used for spatial filtering to achieve continuous spatial variation [41]. As delineated in (9), the Rician factor is modeled to encapsulate the variations of both frequency and bandwidth. This methodology can be extended to the modeling of SF, delay spread, and cross-polarization ratio, ensuring a comprehensive reflection of channel characteristics.

Noted that the proposed model aligns with the cluster delay line model framework. This alignment is particularly evident in the calculation of scattering cluster angles, where the azimuth and elevation angular spreads, with respect to both departure and arrival paths, play a crucial role. The principle of channel reciprocity mandates that swapping the Tx and Rx positions inverses the role of departure and arrival angular spreads, i.e., the departure angular spread at the Tx becomes the arrival angular spread at the Rx and vice versa. Additionally, the angular orientation of each propagation ray, or sub-path, is determined by a specific distribution, reinforcing the fidelity of model to real-world channel behaviors.

B. Bandwidth-correlated Path Numbers

Upon generating spatially-dependent LSPs, the initial positions of scattering clusters and the corresponding path angles are determined. We defined the spatial intervals, where LSPs remain constant and parameters like path power and path phase continue to evolve, as quasi-stationary segments. As the communication system transitions into a new quasi-stationary segment, it dynamically generates scattering clusters based on delay and path angles. Notably, with bandwidth expands to a sufficiently wide extent, channel conditions evolve from their intrinsic randomness to a more deterministic behavior. This phenomenon is indicative of the channel hardening effect, where the variability of channel gains diminishes due to the increased bandwidth [42]. This effect is adequately captured in the proposed model, which considers both frequency and bandwidth influences. Consequently, the distribution of scattering cluster exhibits distinct patterns under variant frequency and bandwidth conditions during the time-frequency cluster evolution process.

In this paper, we employ the RT technology to obtain the number of scattering clusters $N(t,B)$. The RT technique leverages principles of geometrical optics and electromagnetic wave propagation, involving scenario reconstruction and assessing whether rays emitted from the transmitter intersect with the geometric triangular facets of scatterers obtained through triangulation. This process facilitates the tracking of each sub-path by identifying points of intersection. Following sub-path generation, we utilize a Kernel-power-density-based clustering algorithm to ascertain the number of clusters and the quantity of sub-paths within each cluster [43]. For each cluster sample x, the algorithm computes the density ρ using the K nearest clusters as follows

$$\begin{aligned} \rho_{\mathrm{x}} = {} & \sum_{y \in K_x} \exp\left(P_y\right) \exp\left(- \frac{\left|\tau_x - \tau_y\right|}{\left(\sigma_\tau\right)^2} \right) \\ & \cdot \exp\left(- \frac{\left|\phi_x^{\mathrm{T}} - \phi_y^{\mathrm{T}}\right|}{\left(\sigma_\phi^{\mathrm{T}}\right)} \right) \exp\left(- \frac{\left|\phi_x^{\mathrm{R}} - \phi_y^{\mathrm{R}}\right|}{\left(\sigma_\phi^{R}\right)} \right) \end{aligned} \tag{10}$$

where P_y is the power of another arbitrary sub-path, $\tau_{x/y}$ is the delay of sub-path, $\sigma_{(\cdot)}$ denotes the standard deviation of the sub-paths, $\phi^{\mathrm{T}}_{x/y}$ and $\phi^{\mathrm{R}}_{x/y}$ represent the azimuth angle of departure or arrival in the clustering process. It is noteworthy that the kernel density in equation (10) can be

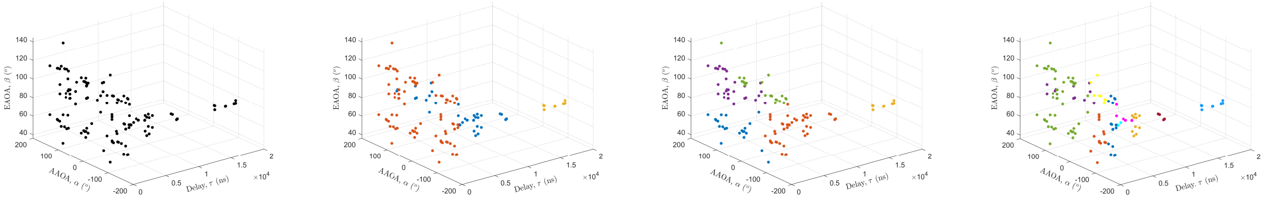

(a) B=10 MHz (b) B=30 MHz (c) B=500 MHz (d) B=1 GHz

Fig. 3. Clustering procedure with various bandwidths.

adjusted as necessary. For instance, if consideration of the elevation domain is required, corresponding kernel density functions for elevation angle of departure and elevation angle of arrival may be incorporated. Utilizing the Kernel-power-density-based clustering algorithm, rays are categorized into distinct clusters, enabling the determination of both path number $N(t, B)$ and sub-path number M_n. Fig. 3 illustrates this process, where different colors in the sub-figures represent varied clustering outcomes derived from the same set of scattering path data produced by RT technique. In scenarios with narrow communication bandwidth, depicted in sub-figure (a), the limited temporal resolution renders it challenging to differentiate between sub-paths. Consequently, all sub-paths are grouped into a single cluster, leading to multipath fading. As communication bandwidth increases, as shown from sub-figures (b) to (d), the resolution of time delays enhances, progressively allowing for the identification of an increased number of distinct paths. Simultaneously, the number of sub-paths within each cluster decreases, contributing to a reduction in the severity of fading for each path, i.e., the channel hardening phenomenon.

This methodology for determining the path and sub-path number parameters effectively captures the impact of bandwidth, offering an accurate depiction of its influence on ultra-wideband channels. Specifically, the total number of sub-paths should be a constant which is user-defined, depending on the required computational accuracy. When channel bandwidth change, the proposed model updates the path number $N(t, B)$ and the n^{th} sub-path number M_n according to the clustering procedure based on RT method.

C. Delay-posture-correlated Path Power

The path power describes the amplitude intensity of a signal along specific propagation paths, distinguishing between LoS and NLoS components. Traditionally, channel models normalize the power of the LoS component, with the NLoS path power being significantly influenced by path delay. In the proposed model, the impact of posture variation is taken into account, and a multi-bounce parameter evolution method is given, enhancing the realism of the proposed model. For the LoS component, the delay is deterministically calculated based on the geometric relationship between the Tx and Rx. Accurate channel parameters for MIMO systems necessitate performing these calculations for each element within an antenna array. Initially, the instantaneous location vector for either the Tx or Rx can be expressed as

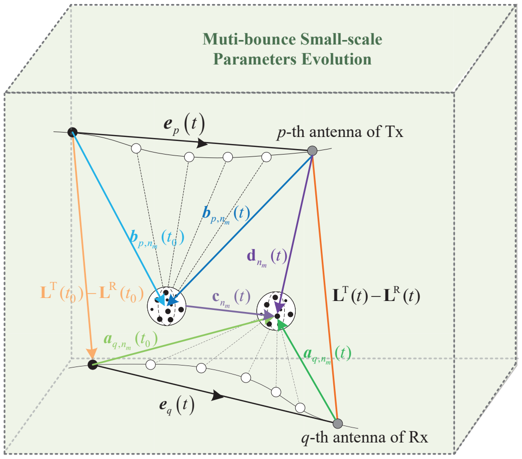

Fig. 4. Muti-bounce small-scale parameters evolution approach.

$$\mathbf{L}^{\text{T/R}}(t) = \mathbf{L}^{\text{T/R}}(t_0) + \int_{t_0}^{t} \mathbf{v}^{\text{T/R}}\left(t'\right) dt' \tag{11}$$

where $\mathbf{L}^{\text{T/R}}(t_0)$ denotes the initial location of Tx and Rx. Then, the delay of LoS path can be calculated directly by the ratio of distance to wave speed as

$$\tau_{pq}^{\text{L}}(t) = \left\| \left(\mathbf{L}^{\text{T}}(t) + \mathbf{e}_p(t)\right) - \left(\mathbf{L}^{\text{R}}(t) + \mathbf{e}_q(t)\right) \right\| / c \tag{12}$$

where $\mathbf{e}_p(t)$ and $\mathbf{e}_q(t)$ are the vector pointing to the p^{th} and q^{th} antenna element from the centers of Tx and Rx, respectively, c is the wave velocity.

The calculation of NLoS path delays incorporates topology data involving the Tx, Rx, the first -bounce scatterer (FBS), and the last-bounce scatterer (LBS). Fig. 4 depicts the evolution of multi-bounce small-scale parameters within the proposed model. We designate $\mathbf{a}_{q,n_m}(t)$ as the vector from the position of q^{th} antenna element of the Rx to the location of the LBS at a given time t. Conversely, vector $\mathbf{b}_{p,n_m}(t)$ points to the FBS from the p^{th} antenna element of the Tx, and $\mathbf{c}_{n_m}(t)$ is the vector connecting the FBS to the LBS. This configuration outlines that the signal propagation path is constituted by the aforementioned three vectors. Moreover, the total NLoS signal propagation delay can be expressed as

$$\tau_{pq,n_m}^{\text{NL}}(t) = \left(\|\mathbf{a}_{q,n_m}(t)\| + \|\mathbf{b}_{p,n_m}(t)\| + \|\mathbf{c}_{n_m}(t)\|\right)/c. \tag{13}$$

It is evident from the illustration that a triangle is formed by the p^{th} antenna element, the q^{th} antenna element, and either

$$\left\|\mathbf{b}_{p,n_m}(t)\right\| = \frac{\left(\tau_{pq}^{\mathrm{L}}(t)\cdot c + \left\|\mathbf{L}^{\mathrm{T}}(t_0)-\mathbf{L}^{\mathrm{R}}(t_0)\right\| - \left\|\mathbf{a}_{q,n_m}(t)\right\|\right)^2 - \left\|\mathbf{d}_{n_m}(t)\right\|^2}{2\cdot\left(\tau_{pq}^{\mathrm{L}}(t)\cdot c + \left\|\mathbf{L}^{\mathrm{T}}(t_0)-\mathbf{L}^{\mathrm{R}}(t_0)\right\| - \left\|\mathbf{a}_{q,n_m}(t)\right\| - \mathbf{d}_{n_m}(t)\mathbf{b}_{p,n_m}(t)/\left\|\mathbf{b}_{p,n_m}(t)\right\|\right)} \tag{17}$$

the FBS or LBS. However, these two triangular configurations alone do not suffice to solve an equation involving the three vectors. A common strategy for this dilemma is to apply a Gaussian random process for generating the length of vector $\mathbf{c}_{n_m}(t)$, simulating the random multi-bounce path among scatterers (referred to as the virtual-link method in [22]). An alternative method for overcoming extra degree of freedom in the equation is to employ optimization techniques, minimizing the length of $\mathbf{c}_{n_m}(t)$ to deduce the lengths of $\mathbf{a}_{q,n_m}(t)$ and $\mathbf{b}_{p,n_m}(t)$. This approach frames the problem as the following optimization task

$$\begin{aligned} &\min_{|\mathbf{a}|,|\mathbf{b}|} \left\|\mathbf{c}_{n_m}(t)\right\| = \tau_{pq,n_m}^{\mathrm{NL}}(t)\cdot c - \left\|\mathbf{b}_{p,n_m}(t)\right\| - \left\|\mathbf{a}_{q,n_m}(t)\right\| \\ &\text{subject to} \quad \begin{array}{c} \mathbf{L}^{\mathrm{T}}(t_0)-\mathbf{L}^{\mathrm{R}}(t_0)=\mathbf{b}_{p,n_m}(t_0)+\mathbf{c}_{n_m}(t)-\mathbf{a}_{q,n_m}(t_0), \\ \left\|\mathbf{b}_{p,n_m}(t)\right\|\geq d_{\min}, \\ \left\|\mathbf{a}_{q,n_m}(t)\right\|\geq d_{\min}. \end{array} \end{aligned} \tag{14}$$

The minimum distance d_{min} is user-defined variable according to the specific scenario. In U2G communication scenarios, FBS and LBS positions are generally nearer to ground terminals than to aerial ones. Consequently, we assign the value d_{min} to vector $\mathbf{a}_{q,n_m}(t)$ and employ the cosine theorem to ascertain the interrelations among the remaining vectors as (15)-(17)

$$\mathbf{d}_{n_m}(t) = \mathbf{L}^{\mathrm{T}}(t) - \mathbf{L}^{\mathrm{R}}(t) + \mathbf{a}_{q,n_m}(t) \tag{15}$$

$$\mathbf{c}_{n_m}(t) = \mathbf{d}_{n_m}(t) - \mathbf{b}_{p,n_m}(t). \tag{16}$$

The prevalent single-bounce model can be acknowledged as a subset of our comprehensive model. This simplification occurs when the FBS and LBS locations merge, rendering the model equivalent to the conventional single-bounce framework, where $\mathbf{c}_{n_m}(t) = 0$.

Following the derivation of delay parameters, the delay-correlated path power of can be calculated. The power of LoS path is controlled by the Rician factor, indicating the power ratio between LoS and NLoS components. Meanwhile, The power distribution across NLoS paths can be determined as

$$\tilde{C}_{pq,n_m}^{\mathrm{NL}}(t) = \exp\left(-\tau_{pq,n_m}^{\mathrm{NL}}(t)\,\frac{r_\tau - 1}{r_\tau\sigma_\tau}\right)10^{-SF_{\mathrm{c}}/10} \tag{18}$$

where r_τ represents the delay scalar, σ_τ denotes the delay spread, and SF_{c} is the cluster shadow fading obeying the Gaussian distribution. Subsequently, the relative power of the NLoS component can be finalized through a normalization procedure

$$C_{pq,n_m}^{\mathrm{NL}}(t) = \tilde{C}_{pq,n_m}^{\mathrm{NL}}(t) / \sum_{n=1}^{N(t,B)}\sum_{m=1}^{M_n}\tilde{C}_{pq,n_m}^{\mathrm{NL}}(t). \tag{19}$$

Moreover, the impact of posture variation is critical in UAV communication systems. Additional power loss emerges when the airframe structure obstructs the signal, causing signal blockage to the ground receiver during UAV posture changes, as depicted in Fig. 5. Based on the positions of the UAV and the ground terminal, the LoS direction vector $\mathbf{s}_l^{\mathrm{T}}(t)$ and the angle of departure $\beta_l^{\mathrm{T}}(t)$ can be determined. Furthermore, we introduce a vector set $\mathbf{\Theta}^{\mathrm{E}}$ comprising all direction vectors from the airframe edge to the antenna elements. $\mathbf{\Theta}^{\mathrm{E}}\left(\mathbf{s}_l^{\mathrm{T}}(t)\right)$ is the vector matching the azimuth angle of $\mathbf{s}_l^{\mathrm{T}}(t)$, which determines the angle $\theta^{\mathrm{E}}(t)$. The angle $\theta^{\mathrm{P}}(t)$ incorporates the UAV posture variation, which depends on the posture matrix $\mathbf{R}^{\mathrm{P}}(t)$. Consequently, the power modification factor can be modeled as

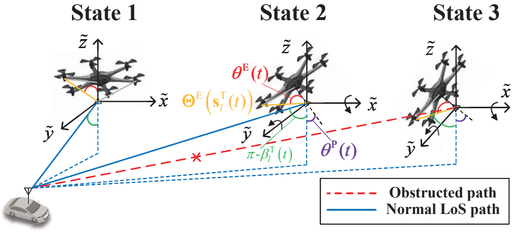

Fig. 5. Addition power loss with different UAV postures.

$$C_{pq}^{\mathrm{L}}(t) = \begin{cases} 1, & \theta^{\mathrm{E}}(t) + \theta^{\mathrm{P}}(t) \geq \beta_l^{\mathrm{T}}(t) \\ 0, & \text{else} \end{cases} \tag{20}$$

where $\theta^{\mathrm{E}}(t)$ is computed through $\theta^{\mathrm{E}}(t) = \left\langle \mathbf{\Theta}^{\mathrm{E}}\left(\mathbf{s}_l^{\mathrm{Tx}}(t)\right), \mathbf{e}_{\tilde{z}}\right\rangle$, with $\mathbf{e}_{\tilde{z}}$ being the base vector of the $\tilde{z}$ axis, $\theta^{\mathrm{P}}(t)$ can be obtained by $\theta^{\mathrm{P}}(t) = \left\langle -\mathbf{e}_{\tilde{z}}\mathbf{R}^{\mathrm{P}}(t), -\mathbf{e}_{\tilde{z}}\right\rangle$. Notably, the power modification factor accounts for posture variations alongside the airframe structure and the transmitter and receiver locations.

D. Frequency-correlated Path Phase

The frequency-correlated path phase caused by the Doppler effect is defined as the equivalent Doppler phase. The first derivative of this phase with respect to time is the Doppler shift. The proposed model calculates the equivalent Doppler phase for each path by considering the relative movement between the transmitter and receiver, the UAV's posture variation, and the carrier frequency. The equivalent Doppler phases can be formulated as

$$\Phi_{pq,f}^{\mathrm{L}}(t) = \mathrm{U}(0,2\pi) + \Phi_{\mathrm{D},pq,f}^{\mathrm{L}}(t) + \Phi_{\mathrm{A},pq,f}^{\mathrm{L}}(t) \tag{21}$$

$$\Phi_{pq,f,n_m}^{\mathrm{NL}}(t) = \mathrm{U}(0,2\pi) + \Phi_{\mathrm{D},pq,f,n_m}^{\mathrm{NL}}(t) + \Phi_{\mathrm{A},pq,f,n_m}^{\mathrm{NL}}(t) \tag{22}$$

where $\Phi_{\mathrm{D},pq,f/\mathrm{D},pq,f,n_m}^{\mathrm{L/NL}}(t)$ denotes phase variations attributable to the dual mobility of the terminals, and $\Phi_{\mathrm{A},pq,f/\mathrm{A},pq,f,n_m}^{\mathrm{L/NL}}(t)$ represents the spatially modified phases for the posture variation within MIMO communication systems.

To analyze the Doppler effect, it is crucial to compute path angles. With the position vectors of the Tx, Rx, FBS, and LBS defined during path delay calculations, the geometric relationships among these vectors allow for the determination of corresponding angles as

$$\alpha_l^{\mathrm{T}}(t)=\arctan_2\left(\frac{\mathbf{e}_{\mathrm{y}}\cdot\left(\mathbf{L}^{\mathrm{R}}(t)+\mathbf{e}_q(t)\right)-\mathbf{e}_{\mathrm{y}}\cdot\left(\mathbf{L}^{\mathrm{T}}(t)+\mathbf{e}_p(t)\right)}{\mathbf{e}_{\mathrm{x}}\cdot(\mathbf{L}^{\mathrm{R}}(t)+\mathbf{e}_q(t))-\mathbf{e}_{\mathrm{x}}\cdot(\mathbf{L}^{\mathrm{T}}(t)+\mathbf{e}_p(t))}\right) \quad (23)$$

$$\beta_l^{\mathrm{T}}(t)=\arcsin\left(\frac{\mathbf{e}_{\mathrm{z}}\cdot\left(\mathbf{L}^{\mathrm{R}}(t)+\mathbf{e}_q(t)\right)-\mathbf{e}_{\mathrm{z}}\cdot\left(\mathbf{L}^{\mathrm{T}}(t)+\mathbf{e}_p(t)\right)}{\sqrt{\left\|\mathbf{L}^{\mathrm{R}}(t)+\mathbf{e}_q(t)-\mathbf{L}^{\mathrm{T}}(t)-\mathbf{e}_p(t)\right\|}}\right) \quad (24)$$

$$\alpha_l^{\mathrm{R}}(t)=\pi-\alpha_l^{\mathrm{Tx}}(t) \quad (25)$$

$$\beta_l^{\mathrm{R}}(t)=\pi-\beta_l^{\mathrm{T}}(t) \quad (26)$$

$$\alpha_{n_m}^{\mathrm{T}}(t)=\arctan_2\left(\frac{\mathbf{e}_{\mathrm{y}}\cdot\left(\mathbf{L}^{\mathrm{T}}(t)+\mathbf{e}_p(t)+\mathbf{b}_{p,n_m}(t)\right)}{\mathbf{e}_{\mathrm{x}}\cdot\left(\mathbf{L}^{\mathrm{T}}(t)+\mathbf{e}_p(t)+\mathbf{b}_{p,n_m}(t)\right)}\right) \quad (27)$$

$$\beta_{n_m}^{\mathrm{T}}(t)=\arcsin\left(\frac{\mathbf{e}_{\mathrm{z}}\cdot\left(\mathbf{L}^{\mathrm{T}}(t)+\mathbf{e}_p(t)+\mathbf{b}_{p,n_m}(t)\right)}{\sqrt{\left\|\mathbf{L}^{\mathrm{T}}(t)+\mathbf{e}_p(t)+\mathbf{b}_{p,n_m}(t)\right\|}}\right) \quad (28)$$

$$\alpha_{n_m}^{\mathrm{R}}(t)=\arctan_2\left(\frac{\mathbf{e}_{\mathrm{y}}\cdot\left(\mathbf{L}^{\mathrm{R}}(t)+\mathbf{e}_q(t)+\mathbf{a}_{q,n_m}(t)\right)}{\mathbf{e}_{\mathrm{x}}\cdot\left(\mathbf{L}^{\mathrm{R}}(t)+\mathbf{e}_q(t)+\mathbf{a}_{q,n_m}(t)\right)}\right) \quad (29)$$

$$\beta_{n_m}^{\mathrm{R}}(t)=\arcsin\left(\frac{\mathbf{e}_{\mathrm{z}}\cdot\left(\mathbf{L}^{\mathrm{R}}(t)+\mathbf{e}_q(t)+\mathbf{a}_{q,n_m}(t)\right)}{\sqrt{\left\|\mathbf{L}^{\mathrm{R}}(t)+\mathbf{e}_q(t)+\mathbf{a}_{q,n_m}(t)\right\|}}\right). \quad (30)$$

Subsequently, the unit vectors $\mathbf{s}_l^{\mathrm{T}}(t)$, $\mathbf{s}_l^{\mathrm{R}}(t)$, $\mathbf{s}_{n_m}^{\mathrm{T}}(t)$, and $\mathbf{s}_{n_m}^{\mathrm{R}}(t)$ for the LoS and NLoS paths at both the Tx and Rx sides are defined. They can be obtained by converting the AAoD $\alpha_{n_m}^{\mathrm{T}}(t)$, AAoA $\alpha_{n_m}^{\mathrm{R}}(t)$, EAoD $\beta_{n_m}^{\mathrm{T}}(t)$, and EAoA $\beta_{n_m}^{\mathrm{R}}(t)$ into Cartesian coordinates. Utilizing the angle unit vectors, the time-frequency-variant Doppler phase components for LoS and NLoS paths can be obtained by

$$\Phi_{\mathrm{D},pq,f}^{\mathrm{L}}(t)=\frac{2\pi f}{c}\int_0^t\left\|\mathbf{s}_l^{\mathrm{T}}(\tilde{t})\left(\mathbf{v}^{\mathrm{T}}(\tilde{t})-\mathbf{v}^{\mathrm{R}}(\tilde{t})\right)\right\|d\tilde{t} \quad (31)$$

$$\Phi_{\mathrm{D},pq,f,n_m}^{\mathrm{NL}}(t)=\frac{2\pi f}{c}\int_0^t\left\|\mathbf{s}_{n_m}^{\mathrm{T}}(\tilde{t})\mathbf{v}^{\mathrm{T}}(\tilde{t})+\mathbf{s}_{n_m}^{\mathrm{R}}(\tilde{t})\mathbf{v}^{\mathrm{R}}(\tilde{t})\right\|d\tilde{t}. \quad (32)$$

After considering the frequency-variant property due to Doppler effect, it is shown that the rotation of MIMO antenna array is influenced by not only the arbitrary velocity but also the time-variant 3D UAV posture. The revised expressions delineating the antenna phase terms for LoS and NLoS propagation paths are presented as follows

$$\Phi_{\mathrm{A},pq,f}^{\mathrm{L}}(t)=\frac{2\pi f}{c}\left\|\begin{array}{l}\left(\mathbf{L}^{\mathrm{T}}(t)+\mathbf{e}_p(t)\right)\mathbf{R}^{\mathrm{P}}(t)\mathbf{s}_l^{\mathrm{T}}(t)\\+\left(\mathbf{L}^{\mathrm{R}}(t)+\mathbf{e}_q(t)\right)\mathbf{R}^{\mathrm{R}}(t)\mathbf{s}_l^{\mathrm{R}}(t)\end{array}\right\| \quad (33)$$

$$\Phi_{\mathrm{A},pq,f,n_m}^{\mathrm{NL}}(t)=\frac{2\pi f}{c}\left\|\begin{array}{l}\left(\mathbf{L}^{\mathrm{T}}(t)+\mathbf{e}_p(t)\right)\mathbf{R}^{\mathrm{P}}(t)\mathbf{s}_{n_m}^{\mathrm{T}}(t)\\+\left(\mathbf{L}^{\mathrm{R}}(t)+\mathbf{e}_q(t)\right)\mathbf{R}^{\mathrm{R}}(t)\mathbf{s}_{n_m}^{\mathrm{R}}(t)\end{array}\right\| \quad (34)$$

where the velocity rotation matrix $\mathbf{R}^{\mathrm{R}}(t)$ is applied to modify the position vector in line with the changing directions of movement, aligning with the initially established definition [44]. Notably, even in the absence of UAV velocity, posture alterations can still provoke a rotation in the coordinate system. To accurately capture the UAV posture, a specific posture matrix is utilized. The definitions of roll, yaw, and pitch angles is illustrated in Fig. 1. The posture matrix $\mathbf{R}^{\mathrm{P}}(t)$, which maps from the coordinate system of the Tx to that of the Rx, can be expressed as (35). Through modifying the roll, yaw, and pitch angles, i.e., ω, φ, and γ within the defined posture matrix, the posture dynamics of UAV are effectively integrated into the channel model. Consequently, this method ensures an accurate depiction of the posture variations of UAV and precisely adjustments for spatial phase variations.

IV. STATISTICAL PROPERTIES OF U2G CHANNEL

Due to the randomness introduced by the scattering environment in wireless channels, it is essential to analyze channel characteristics and assess channel quality through statistical properties. This chapter will introduce and derive key statistical properties of the channel to further analyze and study the proposed model. Note that we make modifications based on the traditional GBSM statistical properties for more comprehensive analysis.

The STF CF measures the correlation between two channels at different time instants, different frequencies, and different antenna elements. For the sake of clarity, in this section, we refer to $H_{pq,f_c}(t,f,B)$ as $H_{pq}(t,f)$. The STF CF between $H_{pq}(t,f)$ and $H_{\tilde{p}\tilde{q}}(t+\Delta t,f+\Delta f)$ is defined as

$$\begin{aligned}&R_{pq,\tilde{p}\tilde{q}}\left(t,f;\Delta r^{\mathrm{T}},\Delta r^{\mathrm{R}},\Delta t,\Delta f\right)\\&\quad=\mathrm{E}\left[H_{pq}(t,f)\,H_{\tilde{p}\tilde{q}}^{*}(t+\Delta t,f+\Delta f)\right]\end{aligned} \quad (36)$$

where the expectation operator is denoted as $\mathrm{E}[\cdot]$, the $(\cdot)^*$ indicates the complex conjugate of a function, Δr^{T} and Δr^{R} are the antenna array element spacing at the Tx and Rx, respectively. By substituting (8) into (36), the STF CF is obtained as (37), where the STF CF of LoS and NLoS components are further derived and simplified as (38) and (39), where the f_d^{L} and f_d^{NL} are the equivalent Doppler frequency of LoS and NLoS component, which can be derived through the time differentiation of the phase $\Phi_{pq,f_c}^{\mathrm{L}}(t)$ and $\Phi_{pq,f_c,n_m}^{\mathrm{NL}}(t)$.

When the channel is wide-sense stationary in the time domain, the temporal correlation function (TCF) can be obtained by setting $\Delta r^{\mathrm{T}}=0$, $\Delta r^{\mathrm{R}}=0$, and $\Delta f=0$, which implies that the same antenna elements are used at both the Tx and Rx, the TCF can be obtained by (40). Similarly, the FCF describes the correlation of the channel in the frequency domain. By setting $\Delta r^{\mathrm{T}}=0$, $\Delta r^{\mathrm{R}}=0$, $\Delta t=0$, the FCF can be expressed as (41).

The PDP, also known as delay power spectrum density (Delay PSD), characterizes the channel power spectrum as a function of variable delay τ. PDP is the inverse Fourier transform of FCF $R_{pq}(t,f;\Delta f)$ with respect to Δf. It can be determined by the following expression

$$S_{pq}(t,f;\tau)=\int_{-\infty}^{\infty}R_{pq}(t,f;\Delta f)\,e^{j2\pi\tau\Delta f}d\Delta f. \quad (42)$$

Given the limited bandwidth of transceiver equipment in real-world scenarios, the minimum frequency separation Δf corresponds to discrete path delay $\tau_{pq,n_m}(t)$. Consequently, the

$$\mathbf{R}^{\mathrm{P}}(t)=\begin{bmatrix}\cos\omega\cos\varphi & \cos\omega\sin\varphi\sin\gamma-\sin\omega\cos\gamma & \cos\omega\sin\varphi\cos\gamma+\sin\omega\sin\gamma\\ \sin\omega\cos\varphi & \sin\omega\sin\varphi\sin\gamma+\cos\omega\cos\gamma & \sin\omega\sin\varphi\cos\gamma-\cos\omega\sin\gamma\\ -\sin\varphi & \cos\varphi\sin\gamma & \cos\varphi\cos\gamma\end{bmatrix} \tag{35}$$

$$\begin{aligned} R_{pq,\tilde{p}\tilde{q}}\left(t,f;\Delta r^{\mathrm{T}},\Delta r^{\mathrm{R}},\Delta t,\Delta f\right)=&\sqrt{\frac{K_{f_c}\left(t,B\right)}{K_{f_c}\left(t,B\right)+1}\cdot\frac{K_{f_c+\Delta f}\left(t+\Delta t,B\right)}{K_{f_c+\Delta f}\left(t+\Delta t,B\right)+1}}R^{\mathrm{L}}_{pq,\tilde{p}\tilde{q}}\left(t,f;\Delta r^{\mathrm{T}},\Delta r^{\mathrm{R}},\Delta t,\Delta f\right)\\ &+\sqrt{\frac{1}{K_{f_c}\left(t,B\right)+1}\cdot\frac{1}{K_{f_c+\Delta f}\left(t+\Delta t,B\right)+1}}R^{\mathrm{NL}}_{pq,\tilde{p}\tilde{q}}\left(t,f;\Delta r^{\mathrm{T}},\Delta r^{\mathrm{R}},\Delta t,\Delta f\right)\end{aligned} \tag{37}$$

$$R^{\mathrm{L}}_{pq,\tilde{p}\tilde{q}}\left(t,f;\Delta r^{\mathrm{T}},\Delta r^{\mathrm{R}},\Delta t,\Delta f\right)=C^{\mathrm{L}}_{pq}\left(t\right)C^{\mathrm{L}}_{\tilde{p}\tilde{q}}\left(t+\Delta t\right)e^{j2\pi\left(\left(f^{\mathrm{L}}_{d}-f\right)\tau^{\mathrm{L}}_{pq}(t)-\left(f^{\mathrm{L}}_{d}-f+\Delta f\right)\tau^{\mathrm{L}}_{\tilde{p}\tilde{q}}(t+\Delta t)\right)} \tag{38}$$

$$R^{\mathrm{NL}}_{pq,\tilde{p}\tilde{q}}\left(t,f;\Delta r^{\mathrm{T}},\Delta r^{\mathrm{R}},\Delta t,\Delta f\right)=\mathrm{E}\left[\sum_{n=1}^{N(t,B)}\sum_{m=1}^{M_n}C^{\mathrm{NL}}_{pq,n_m}\left(t\right)C^{\mathrm{NL}}_{\tilde{p}\tilde{q},n_m}\left(t+\Delta t\right)\ e^{j2\pi\left(\left(f^{\mathrm{NL}}_{d}-f\right)\tau^{\mathrm{NL}}_{pq}(t)-\left(f^{\mathrm{NL}}_{d}-f+\Delta f\right)\tau^{\mathrm{NL}}_{\tilde{p}\tilde{q}}(t+\Delta t)\right)}\right] \tag{39}$$

$$\begin{aligned} R_{pq}\left(t,f;\Delta t\right)=&\sqrt{\frac{K_{f_c}\left(t,B\right)}{K_{f_c}\left(t,B\right)+1}\cdot\frac{K_{f_c+\Delta f}\left(t+\Delta t,B\right)}{K_{f_c+\Delta f}\left(t+\Delta t,B\right)+1}}e^{\mathrm{j}2\pi\left(f^{\mathrm{L}}_{d}-f\right)\tau^{\mathrm{L}}_{pq}(t)\tau^{\mathrm{L}}_{pq}(t+\Delta t)}\\ &+\sqrt{\frac{1}{K_{f_c}\left(t,B\right)+1}\cdot\frac{1}{K_{f_c+\Delta f}\left(t+\Delta t,B\right)+1}}\mathrm{E}\left[\sum_{n=1}^{N(t.B)}\sum_{m=1}^{M_n}C^{\mathrm{NL}}_{pq,n_m}\left(t\right)e^{\mathrm{j}2\pi\left(f^{\mathrm{NL}}_{d}-f\right)\left(\tau^{\mathrm{NL}}_{pq}(t)-\tau^{\mathrm{NL}}_{pq}(t+\Delta t)\right)}\right]\end{aligned} \tag{40}$$

$$\begin{aligned} R_{pq}\left(t,f;\Delta f\right)=&\sqrt{\frac{K_{f_c}\left(t,B\right)}{K_{f_c}\left(t,B\right)+1}\cdot\frac{K_{f_c+\Delta f}\left(t+\Delta t,B\right)}{K_{f_c+\Delta f}\left(t+\Delta t,B\right)+1}}e^{-j2\pi\Delta f\tau^{\mathrm{L}}_{pq}(t)}\\ &+\sqrt{\frac{1}{K_{f_c}\left(t,B\right)+1}\cdot\frac{1}{K_{f_c+\Delta f}\left(t+\Delta t,B\right)+1}}\mathrm{E}\left[\sum_{n=1}^{N(t,B)}\sum_{m=1}^{M_n}C^{\mathrm{NL}}_{pq,n_m}\left(t\right)\ e^{j2\pi\Delta f\tau^{\mathrm{NL}}_{pq}(t)}\right]\end{aligned} \tag{41}$$

PDP can be calculated involving bandwidth-related parameters as

$$S_{pq}\left(t,f;\tau\right)=\sum_{n=1}^{N(t,B)}\sum_{m=1}^{M_n}P_{pq,n_m}\left(t,f\right)\delta\left(\tau-\tau_{pq,n_m}(t)\right). \tag{43}$$

Note that the two expressions of PDP can be derived from each other. Here, $P_{qp,n_m}(t,f)$ are the received powers for each delay $\tau_{pq,n_m}(t)$, which are affected by the STF evolution of the clusters in space, time, and frequency domains, and will further affect the delay PDP. It should be noted that when the frequency point is fixed, equation (44) reduces to the traditional one as shown in [40].

The RMS-DS is defined as the square root of the second-order central moment of the PDP, and can be calculated as

$$\sigma_{\tau,pq}\left(t,f\right)=\sqrt{\frac{\int_0^\infty\left(\tau-u_{pq}\left(t,f;\tau\right)\right)^2S_{pq}\left(t,f;\tau\right)d\tau}{\int_0^\infty S_{pq}\left(t,f;\tau\right)d\tau}} \tag{44}$$

where $u_{\tau,pq}(t;f)$ is the average delay and is also the first-order moment of PDP. Note that we employ a theoretical definition instead of the discrete approximation typically applied in the engineering.

Doppler PSD, which measures the power distribution over the Doppler frequency axis, is the Fourier transform of TCF $R_{pq}\left(t,f;\Delta t\right)$ with respect to the time interval Δt. It can be calculated as

$$\begin{aligned} S_{pq}\left(t,f;f_d\right)=&\int_{-\infty}^{\infty}R^{\mathrm{L}}_{pq}\left(t,f;\Delta t\right)\cdot e^{-j2\pi f^{\mathrm{L}}_{d}}d\Delta t\\ &+\int_{-\infty}^{\infty}R^{\mathrm{NL}}_{pq}\left(t,f;\Delta t\right)\cdot e^{-j2\pi f^{\mathrm{NL}}_{d}}d\Delta t\end{aligned} \tag{45}$$

where the equivalent Doppler frequencies are employed, enabling the proposed model to accurately reflect the phase shifts resulting from variations in the UAV posture, thereby aligning more closely with the actual circumstances.

V. NUMERICAL RESULTS AND DISCUSSIONS

In this section, we analyze key statistical properties of the proposed UWB U2G channel model via numerical simulations, setting appropriate model parameters for the targeted scenarios. In order to better highlight the bandwidth characteristics, we apply the same motion trajectory in the simulations, so as to eliminate the randomness caused by the motion of terminals. The UAV and the ground terminal are equipped with the omnidirectional dipole antenna, and the antenna pattern is shown in Fig. 6. The carrier frequency is 28 GHz, the scenario is setted as micro-cell urban in simulations.

TABLE II: Channel Simulation Settings

Description	Value
Carrier frequency f_c	28 (GHz)
Initial location of Tx and Rx $\mathbf{L}^{\mathbf{T/R}}(t_0)$	[0 0 150] and [0 0 1.5] (m)
Velocity of Tx/Rx $\mathrm{V}^{\mathrm{T/R}}$	10 and 20 (m/s)
Antenna type	Omnidirectional antenna
Antenna gain	0 dBm
Track type of Tx and Rx	Circular and Uniform Linear
Azimuth of arrival angle spread	1.73 [log10(deg)]
Azimuth of departure angle spread	1.21 [log10(deg)]
Elevation of departure angle spread	0.83 [log10(deg)]
Elevation of arrival angle spread	0.73 [log10(deg)]
Mean and variance of delay spread	-7.14 and 0.38 [log10(s)]

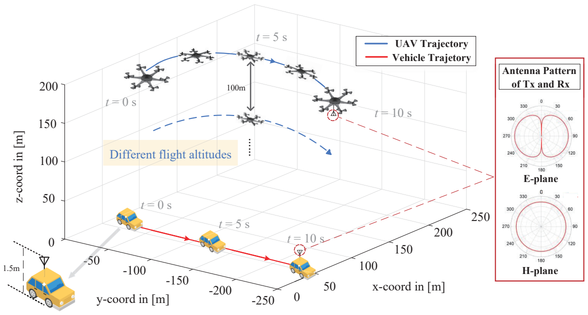

Fig. 6. Antenna pattern and trajectories of two mobile terminals.

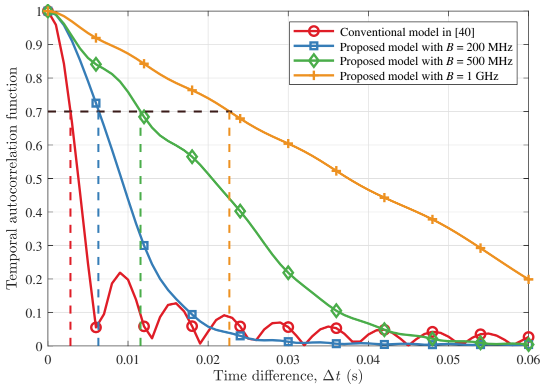

Fig. 7. Comparison of TCFs between conventional model and the proposed model.

Fig. 7 compares the simulated TCFs based on the conventional model in [40] and the proposed model for the U2G channel. The conventional model does not fully account for the influence of bandwidth, limiting its ability to simulate various frequency ranges. The simulation results show that the proposed model demonstrates a less pronounced decline in TCF as bandwidth increases, indicating extended coherence times. This is due to enhanced resolution with increased bandwidth, making the channel more deterministic. As a result, channel similarities over equivalent time spans are enhanced, improving channel correlation and causing a more gradual TCF decline. Specifically, at a TCF of 0.7, the normalized time delays for each curve in the figures are 0.0028, 0.0063, 0.0116, and 0.0227 seconds. These findings highlight the significant impact of bandwidth on TCF in U2G channel models.

Fig. 8 illustrates the FCFs of the proposed model for bandwidths of 20 MHz, 200 MHz, 500 MHz, and 1 GHz, centered at 28 GHz. As the normalized frequency difference increases, the FCFs across different bandwidths exhibit a nearly identical trend of decline and fluctuation. Notably, when the bandwidth is wider, the relative coherence bandwidth diminishes. This indicates that an increase in bandwidth enhances the frequency selectivity of the channel, thus lowering frequency correlation. These findings align with the established behavior of frequency-selective channels and highlight the impact of ultra-wideband technology on coherence bandwidth.

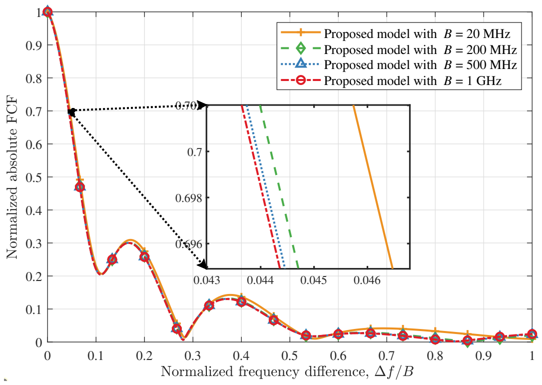

Fig. 8. Impact of various bandwidths on FCF of the proposed model.

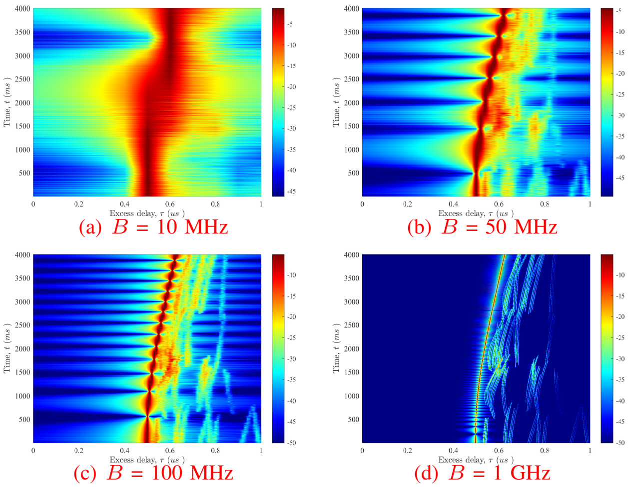

(a) B = 10 MHz (b) B = 50 MHz

(c) B = 100 MHz (d) B = 1 GHz

Fig. 9. Impact of various bandwidths on PDP of the proposed model.

Fig. 9 delineates the variation trends of the PDP under diverse channel bandwidths. Notably, continuous variations manifest in the delay and power of multipath components. The LoS component persistently exhibits relatively high energy, while scattering clusters born and die at different time intervals. Due to the constant initial distance between the Tx and Rx, the LoS path delay stabilizes around 0.5 μs as bandwidth exceeds 1 GHz. Increasing bandwidth leads to a more concentrated power distribution among multipath components, attributable to the enhanced resolution of wideband receiving systems for multipath signals. Consequently, signal fading becomes less pronounced, highlighting the significant influence of bandwidth on the PDP, which is indicative of channel hardening effect.

Fig. 10 demonstrates the impact of relative motion and signal bandwidth on the DPSD in the proposed model. The Doppler shift varies over time due to movement between the transmitter and receiver, as well as changes of the UAV's posture. When comparing a narrowband channel at 10 MHz with a wideband channel at 1 GHz, the figure reveals obvious differences in the DPSD shape as frequency shifts occur. This is because the model accounts for Doppler shifts across different frequencies when calculating the effective Doppler phase. With a narrower bandwidth, the Doppler shift remains relatively stable, resulting in minimal changes to the DPSD shape. However, with a wider bandwidth, the Doppler shift has a more pronounced effect on the DPSD shape. These

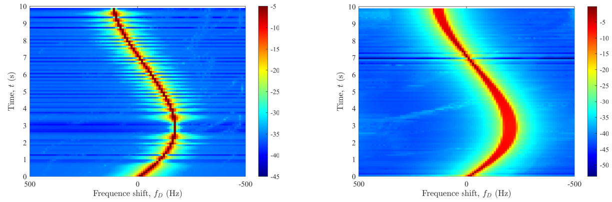

(a) B = 10 MHz (b) B = 1 GHz

Fig. 10. Impact of various bandwidths on DPSD of the proposed model.

findings are particularly relevant for the design of UWB communication systems, where managing Doppler shifts is critical.

To elucidate the influence of ultra-wideband attributes on the channel, we introduce an indicator, termed EV, to quantify the fluctuation degree of the frequency-domain signal as bandwidth varies. Assuming the transmission of an equivalent baseband CIR with unit energy between the Tx and Rx $\hat{h}(t) = \sqrt{B}\text{sinc}(Bt)$, the received energy can be represented as

$$\varepsilon = \frac{1}{B}\int_{-\frac{B}{2}}^{\frac{B}{2}} \left|H_{pq}\left(t,f\right)\right|^2 df. \tag{46}$$

With a normalized ensemble average $\text{E}\left[\varepsilon\right] = 1$, the ensemble variance can be calculated as [45]

$$\begin{aligned}{\sigma_\varepsilon}^2 &= \text{E}[\varepsilon^2] - 1 = \frac{2}{B}\left[\int\limits_0^B \left[R_{pq}\left(t,f;\Delta f\right)\right]^2 \left(1 - \frac{\Delta f}{B}\right) d\Delta f\right] - 1 \\ &= \sum_n \sum_{n' \neq n} P_{pq,n}(t,f) P_{pq,n'}(t,f) \text{sinc}^2\left[B\left(\tau_{pq,n}^{\text{NL}}(t) - \tau_{pq,n'}^{\text{NL}}(t)\right)\right]\end{aligned} \tag{47}$$

where indistinct sub-paths are disregarded. Employing the upper bound $\text{sinc}^2(x) \leq 1/(\pi^2 x^2)$, the EV can be obtained by

$${\sigma_\varepsilon}^2 = \frac{1}{\pi^2 B^2}\sum_n \sum_{n' \neq n} \frac{P_{pq,n}(t,f) P_{pq,n'}(t,f)}{\left(\tau_{pq,n}^{\text{NL}}(t) - \tau_{pq,n'}^{\text{NL}}(t)\right)^2}. \tag{48}$$

Fig. 11 illustrates the EV of the proposed model across varying Rician factors. As bandwidth B in (49) cannot be zero, simulations start with 1 MHz. Higher Rician factors indicate stronger LoS component, corresponding to improved communication environments. With Rician factors of 1, 10, and 20, the respective rates of EV decline progressively increase, eventually stabilizing after decreases of 33 dB, 37.81 dB, and 40.42 dB. This demonstrates the significant impact of the Rician factor on EV. Furthermore, it is observed that EV gradually diminishes with bandwidth increase, signifying a shift towards more deterministic channel fading behavior, i.e., the channel hardening effect.

To demonstrate the effectiveness and accuracy of the proposed model, we compare its simulation results with measured data from measurements in [46]. The carrier frequency is set at 2.585 GHz, with measurements conducted at altitudes above 30m (high altitude) and below 30m (low altitude), where the UAV flies linearly in the horizontal direction at a speed of 5.6 m/s. Fig. 12 illustrates the cumulative distribution functions (CDFs) of the delay spreads on a logarithmic scale for both the proposed model and the measurement data. It is observed that,

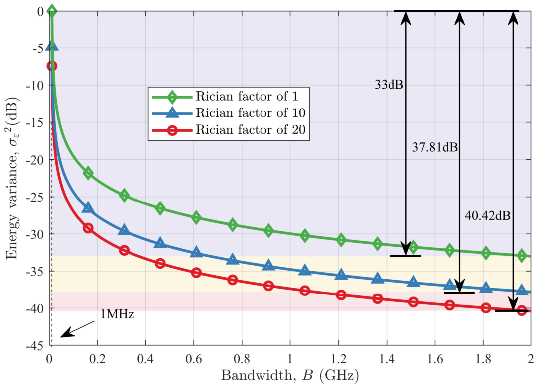

Fig. 11. Energy variance of proposed model with various Rician factor.

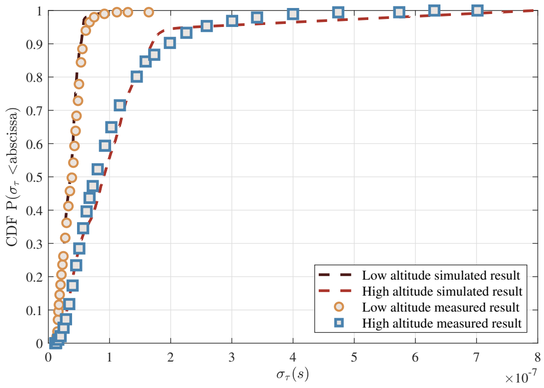

Fig. 12. Comparison of RMS-DSs between the proposed model and measured data.

under matching transmitter-receiver distances and movement speeds, the distribution of the RMS-DS from the proposed model closely aligns with the actual measurements, thus validating the model's accuracy and its support for UAV altitude variations.

Fig. 13 compares the simulated Rician factor of the proposed model with measurement results in [47] across various bandwidths. Under the same scenario settings, it is observed that the cumulative distribution of the normalized Rx power is more dispersed at narrower bandwidth. As bandwidth increases, the normalized Rx power distribution becomes more concentrated. This concentration is a manifestation of channel

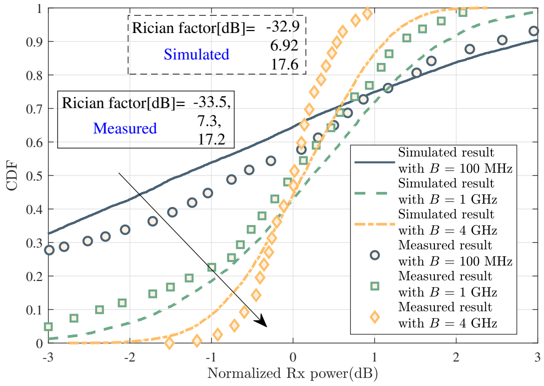

Fig. 13. Comparison of Rician factors between the proposed model and measurement data.

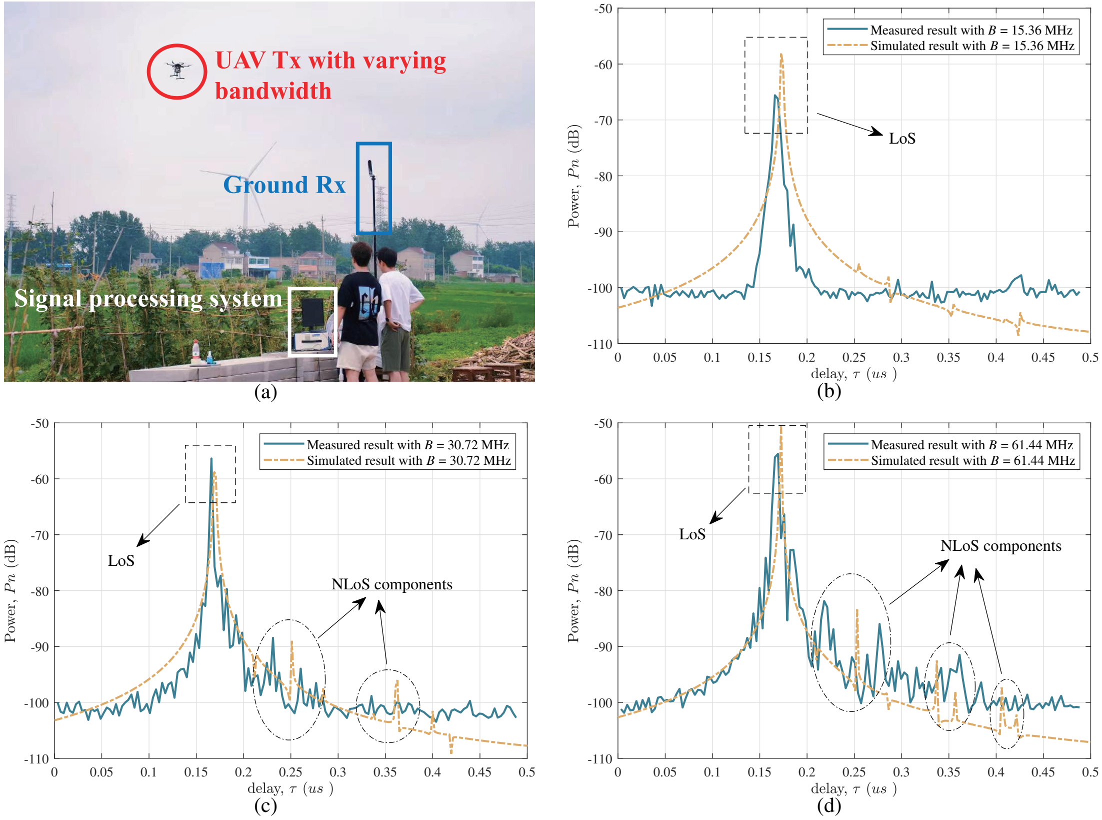

(a)
(b)
(c)
(d)

Fig. 14. Measurement setup and results with simulated outcomes.

hardening, which attributed to increased bandwidth that reducing channel randomness. We also marked the Rician factors calculated from measured results as -32.9, 6.92, and 17.6, while the simulated Rician factors from the proposed model are -33.5, 7.3, and 17.2, respectively.

To validate the accuracy of the proposed model, a measurement campaign was conducted, with settings and outcomes illustrated in Fig. 14 alongside the simulated results of the proposed model. Considering the limited bandwidth capability of drone-carried transmitting equipment, a test scenario with abundant scatterers was chosen to underscore the impact of bandwidth on channel characteristics. The center frequency for the measurement was set at 3.6 GHz, with the transmitter utilizing a self-developed software-defined radio card, and the receiver being the NI PXI SDR platform [48], [49]. In three distinct measurements, the bandwidth of signal was varied, specifically to 15.36 MHz, 30.72 MHz, and 61.44 MHz. Fig. 14(b) reveals the multipath effect of near scatterers as notably weak, with far scatterers being indiscernible. However, as bandwidth increases, Fig. 14(c, d) demonstrate the successful capture of multipath components from distant scatterers. The larger bandwidth enhances delay resolution, as evidenced by Fig. 14(d) showcasing more multipath components than Fig. 14(c). Aligning experimental parameters and calibrating system delay, the simulated outcomes based on our proposed model closely resonate with empirical data, affirming the model's validity and its support for variant bandwidths.

VI. CONCLUSION

This paper has introduced a comprehensive 3D model for U2G communication channels, which incorporates UWB features and accounts for frequency non-stationarity. The proposed model integrates both large-scale and small-scale fading components, incorporating bandwidth-affected channel parameters and a UAV posture matrix. This approach offers a novel method for accurately representing realistic communication scenarios. Through the derivation of spatial LSPs, bandwidth-correlated path numbers, delay-posture-correlated path power, and frequency-correlated path phase, the model can capture the essential non-stationary characteristics of the channel across both time and frequency domains. The application of RT for determining path numbers and optimization methods for path delays enhances the precision in parameter evolution, ensuring a high degree of reliability in simulated outcomes. The phenomenon of channel hardening has been examined. As the bandwidth increases, the number of scattering clusters rises while the number of sub-paths within each cluster diminishes. The evaluation of the proposed model underscores the significant impact of bandwidth and frequency variations on channel characteristics. The comparison of simulated results with actual measurement data validates the feasibility and effectiveness of the proposed model in depicting U2G communication channels. By addressing the intricate details of UWB U2G communication channels and providing a solid foundation for future investigations, this work contributes to the field of wireless communication and UAV technologies.

References

[1] C.-X. Wang, J. Huang, H. Wang, X.-Q. Gao, X.-H. You, and Y. Hao, “6G wireless channel measurements and models: Trends and challenges,” *IEEE Veh. Technol. Mag.*, vol. 15, no. 4, pp. 22–32, Dec. 2020.

[2] H. Jiang, W. Shi, X. Chen, Q. Zhu and Z. Chen, “High-efficient near-field channel characteristics analysis for large-scale MIMO communication systems,” *IEEE Internet Things J.*, DOI: 10.1109/JIOT.2024.3496434.

[3] IEEE Standard for Low-Rate Wireless Networks–Amendment 1: *Enhanced Ultra Wideband (UWB) Physical Layers (PHYs) and Associated Ranging Techniques,* IEEE Standard 802.15.4z-2020 (Amendment to IEEE Standard 802.15.4-2020), 2020.

[4] C. U. Bas, V. Kristem, R. Wang and A. F. Molisch, “Real-Time Ultra-Wideband Channel Sounder Design for 3–18 GHz,” *IEEE Trans. Commun.*, vol. 67, no. 4, pp. 2995-3008, Apr. 2019.

[5] Z. Lian, W. Zhang, Y. Wang, Y. Su, B. Zhang, B. Jin, and B. Wang, “Physics-based channel modeling for IRS-assisted mmWave Communication systems,” *IEEE Trans. Commun.*, vol. 72, no. 5, pp. 2687-2700, May 2024.

[6] H. Ni, Q. Zhu, B. Hua, K. Mao, Y. Pan, F. Ali et al, “Path Loss and Shadowing for UAV-to-Ground UWB Channels Incorporating the Effects of Built-up Areas and Airframe,” *IEEE Trans. Intell. Transport. Syst.*, vol. 25, no. 11, pp. 17066 - 17077, July 2024.

[7] C. Ruan, Z. Zhang, H. jiang, J. Dang, L. Wu and H. Zhang, “Wideband near-field channel covariance estimation for XL-MIMO systems in the face of beam split,” *IEEE Trans. Veh. Technol.*, DOI: 10.1109/TVT.2024.3471733.

[8] L. Zeng, X. Liao, W. Xie, Z. Ma, B. Xiong, and H. Jiang, “UAV-to-ground channel modeling: (quasi-)closed-form channel statistics and manual parameter estimation,” *China Commun.*, 2024, doi: 10.23919/JCC.ja.2023-0661.

[9] J. Wang, Q. Zhu, Z. Lin, J. Chen, G. Ding, Q. Wu, G. Gu, Q. Gao, “Sparse Bayesian Learning-Based Hierarchical Construction for 3D Radio Environment Maps Incorporating Channel Shadowing,” *IEEE Trans. Wireless Commun.*, early access, 2024, doi: 10.1109/TWC.2024.3416447.

[10] R. Zhang, H. Du, Y. Liu, D. Niyato, J. Kang and S. Sunet, “Interactive AI with Retrieval-Augmented Generation for Next Generation Networking,” *IEEE Network*, doi: 10.1109/MNET.2024.3401159.

[11] X. Chu, C. Briso, D. He, X. Yin, and J. Dou, “Channel modeling for low-altitude UAV in suburban environments based on ray tracer,” in *Proc. 12th Eur. Conf. Antennas Propag. (EuCAP)*, Apr. 2018, pp. 1–5.

[12] H. Jiang, W. Shi, Z. Zhang, C. Panet, Q. Wu and F. Shu et al., “Large-scale RIS enabled air-ground channels: near-field modeling and analysis,” *IEEE Trans. Wireless Commun.*, DOI: 10.1109/TWC.2024.3504839.

[13] H. Chang, C.-X. Wang, Y. Liu et al., “A general 3-D nonstationary GBSM for underground vehicular channels,” *IEEE Trans. Antennas Propag.*, vol. 71, no. 2, pp. 1804-1819, Feb. 2023.

[14] H. Chang, C.-X. Wang, J. Bian, Y. He, R. Feng, Y. Chen, and H. Aggoune, “A novel 3D beam domain channel model for UAV massive MIMO communications,” *IEEE Trans. Wireless Commun.*, vol. 22, no. 8, pp. 5431–5445, Aug. 2023.

[15] L. Zeng, X. Liao, Z. Ma, W. Liu, H. Jiang, and Z. Chen, “Towards more adaptive UAV-to-UAV GBSMs: Introducing the extended vMF distribution,” *IEEE Wireless Commun. Lett.*, early access, 2024.

[16] M. Walter, D. Shutin, M. Schmidhammer, D. W. Matolak and A. Zajic, “Geometric Analysis of the Doppler Frequency for General Non-Stationary 3D Mobile-to-Mobile Channels Based on Prolate Spheroidal Coordinates,” *IEEE Trans. Veh. Technol.*, vol. 69, no. 10, pp. 10419-10434, Oct. 2020.

[17] C. A. Gutiérrez, J. T. Gutiérrez-Mena, J. M. Luna-Rivera, D. U. Campos-Delgado, R. Velázquez and M. Pätzold, “Geometry-Based Statistical Modeling of Non-WSSUS Mobile-to-Mobile Rayleigh Fading Channels,” *IEEE Trans. Veh. Technol.*, vol. 67, no. 1, pp. 362-377, Jan. 2018.

[18] A. Seretis and C. D. Sarris, “An Overview of Machine Learning Techniques for Radiowave Propagation Modeling,” *IEEE Trans. Antennas Propag.*, vol. 70, no. 6, pp. 3970-3985, June 2022.

[19] R. Zhang, H. Du, D. Niyato, J. Kang, Z. Xiong and A. Jamalipouret, “Generative AI for Space-Air-Ground Integrated Networks,” *IEEE Wireless Commun.*, doi: 10.1109/MWC.016.2300547, 2024.

[20] G. Yang, Y. Zhang, Z. He, J. Wen, Z. Ji, and Y. Li, “Machine-learning-based prediction methods for path loss and delay spread in air-to-ground millimetre-wave channels,” *IET Microw. Antennas Propag.*, vol. 13, no. 8, pp. 1113–1121, Apr. 2019.

[21] J. Zhang, L. Liu, Y. Fan, L. Zhuang, T. Zhou, and Z. Piao, “Wireless channel propagation scenarios identification: A perspective of machine learning,” *IEEE Access*, vol. 8, pp. 47797–47806, Mar. 2020.

[22] H. Chang, C.-X. Wang, Y. Liu, J. Huang, J. Sun, W. Zhang, et al., “A novel non-stationary 6G UAV-to-ground wireless channel model with 3-D arbitrary trajectory changes,” *IEEE Internet Things J.*, vol. 8, no. 12, pp. 9865–9877, June 2021.

[23] Z. Lian, Y. Wang, Y. Su, P. Ji, L. Ling, Z. Zhang et al., ”A novel beam channel model and capacity analysis for UAV-enabled millimeter-wave communication systems,” IEEE Trans. Wireless Commun., vol. 23, no. 4, pp. 3617-3632, Apr. 2024.

[24] Z. Ma, B. Ai, R. He, G. Wang, Y. Niu, M. Yang, et al., “Impact of UAV rotation on MIMO channel characterization for air-to-ground communication systems,” *IEEE Trans. Veh. Technol.*, vol. 69, no. 11, pp. 12418–12431, Nov. 2020.

[25] Z. Ma, B. Ai, R. He, H. Mi, M. Yang, N. Wang, et al., “Modeling and analysis of MIMO multipath channels with aerial intelligent reflecting surface,” *IEEE J. Select. Areas Commun.*, vol. 40, no. 10, pp. 3027-3040, Oct. 2022.

[26] R. Sun, D. W. Matolak, and W. Rayess, “Air-ground channel characterization for unmanned aircraft systems—Part IV: Airframe shadowing,” *IEEE Trans. Veh. Technol.*, vol. 66, no. 9, pp. 7643-7652, Sept. 2017.

[27] M. Banagar, H. S. Dhillon and A. F. Molisch, “Impact of UAV Wobbling on the Air-to-Ground Wireless Channel,” *IEEE Trans. Veh. Technol.*, vol. 69, no. 11, pp. 14025-14030, Nov. 2020.

[28] S. Yang, Z. Zhang, J. Zhang, and J. Zhang, “Impact of rotary-wing UAV wobbling on millimeter-wave air-to-ground wireless channel,” *IEEE Trans. Veh. Technol.*, vol. 71, no. 9, pp. 9174–9185, Sept. 2022.

[29] X. Yang, D. Zhai, R. Zhang, L. Liu, F. R. Yu, and C. C. M. Leung, “Temporal correlation characteristics of air-to-ground wireless channel with UAV wobble,” *IEEE Trans. Intell. Transp. Syst.*, vol. 24, no. 10, pp. 10702–10715, Oct. 2023.

[30] B. Hua, H. Ni, Q. Zhu, C.-X. Wang, T. Zhou, K. Mao, et al., “Channel modeling for UAV-to-ground communications with posture variation and fuselage scattering effect,” *IEEE Trans. Commun.*, vol. 71, no. 5, pp. 3103-3116, May 2023.

[31] W. Khawaja, O. Ozdemir, F. Erden, I. Guvenc, and D. W. Matolak, “Ultra-wideband air-to-ground propagation channel characterization in an open area,” *IEEE Trans. Aerosp. Electron. Syst.*, vol. 66, no. 6, pp. 4533–4555, Dec. 2020.

[32] Z. Cui, C. Briso-Rodríguez, K. Guan, and Z. Zhong, “Ultra-wideband air-to-ground channel measurements and modeling in hilly environment,” in *Proc. IEEE Int. Conf. Commun. (ICC)*, Dublin, Ireland, 2020, pp. 1–6.

[33] F. Zhang and W. Fan, “Near-Field Ultra-Wideband mmWave Channel Characterization Using Successive Cancellation Beamspace UCA Algorithm,” *IEEE Trans. Vehi. Technol.*, vol. 68, no. 8, pp. 7248-7259, Aug. 2019.

[34] C. Briso, C. Calvo, and Y. Xu, “UWB propagation measurements and modelling in large indoor environments,” *IEEE Access*, vol. 7, pp. 41913–41920, 2019.

[35] V. Kristem, C. U. Bas, R. Wang, and A. F. Molisch, “Outdoor wideband channel measurements and modeling in the 3–18 GHz band,” *IEEE Trans. Wireless Commun.*, vol. 17, no. 7, pp. 4620–4633, July 2018.

[36] K. Guan, B. Peng, D.He, J. M. Eckhardt, H. Yi, S. Rey, et al., “Channel sounding and ray tracing for intrawagon scenario at mmWave and sub-mmWave bands,” *IEEE Trans. Antennas Propag.*, vol. 69, no. 2, pp. 1007–1019, Feb. 2021.

[37] A. Colpaert, Z. Cui, E. Vinogradov, and S. Pollin, “3D non-stationary channel measurement and analysis for MaMIMO-UAV communications,” *IEEE Trans. Veh. Technol.*, vol. 73, no. 5, pp. 6061-6072, May 2024.

[38] B. M. Hochwald, T. L. Marzetta, and V. Tarokh, “Multiple-antenna channel hardening and its implications for rate feedback and scheduling,” *IEEE Trans. Inf. Theory*, vol. 50, no. 9, pp. 1893–1909, Sept. 2004.

[39] P. Zhang, C. Yi, B. Yang, C.-X. Wang, H. Wang, and X.-H. You, “Inbuilding coverage of millimeter-wave wireless networks from channel measurement and modeling perspectives,” *Sci. China Inf. Sci.*, vol. 63, no. 8, pp. 1–16, Aug. 2020.

[40] C.-X. Wang, Z. Lv, X. Gao, X.-H. You, Y. Hao, and H. Haas, “Pervasive wireless channel modeling theory and applications to 6G GBSMs for all frequency bands and all scenarios,” *IEEE Trans. Veh. Technol.*, vol. 71, no. 9, pp. 9159–9173, Sept. 2022.

[41] S. Jaeckel, *“QuaDRiGa—Quasi deterministic radio channel generator, user manual and documentation,”* Fraunhofer Heinrich Hertz Institute, Berlin, Germany, Tech. Rep. V2.6.1, 2021.

[42] T. S. Rappaport, K. A. Remley, C. Gentile, A. F. Molisch, and A. Zajic, *Radio Propagation Measurements and Channel Modeling: Best Practices for Millimeter-Wave and Sub-Terahertz Frequencies.* Cambridge, U.K.: Cambridge Univ. Press, 2021.

[43] R. He, Q. Li, B. Ai, Y. L.-A. Geng, A. F. Molisch, K. Vinod, et al., “A kernel-power-density-based algorithm for channel multipath

components clustering," *IEEE Trans. Wireless Commun.*, vol. 16, no. 11, pp. 7138–7151, Nov. 2017.

[44] K. Mao, Q. Zhu, M. Song, H. Li, B. Ning, G. F. Pedersen, W. Fan, "Machine learning-based 3D channel modeling for U2V mmWave communications," *IEEE Internet Things J.*, vol. 9, no. 18, pp. 17592–17607, Mar. 2022.

[45] M. V. Clark and L. J. Greenstein, "The relationship between fading and bandwidth for multipath channels," *IEEE Trans. Wireless Commun.*, vol. 4, no. 4, pp. 1372–1376, July 2005.

[46] X. Cai, J. Rodríguez-Piñeiro, X. Yin, N. Wang, B. Ai, G. F. Pedersen, et al., "An empirical air-to-ground channel model based on passive measurements in LTE," *IEEE Trans. Veh. Technol.*, vol. 68, no. 2, pp. 1140–1154, Feb. 2019.

[47] N. Iqbal, C. Schneider, J. Luo, D. Dupleich, R. Müller, S. Haefner, et al., "On the stochastic and deterministic behavior of mmWave channels," in *Proc. 11th Eur. Conf. Antennas Propag. (EuCAP)*, Mar. 2017, pp. 1813-1817.

[48] K. Mao, Q. Zhu, C.-X. Wang, X. Ye, J. Gomez-Ponce, X. Cai, et al., "A survey on channel sounding technologies and measurements for UAV-assisted communications," *IEEE Trans. Instrum. Meas.*, Vol.73, pp.1-24, Aug. 2024.

[49] K. Mao, Q. Zhu, Y. Qiu, X. Liu, M. Song, W. Fan, et al., "A UAV-aided real-time channel sounder for highly dynamic nonstationary A2G scenarios," *IEEE Trans. Instrum. Meas.*, vol. 72, pp. 1-15, Aug. 2023.